IEEE Access
Multidisciplinary | Rapid Review | Open Access Journal

Received October 21, 2020, accepted November 30, 2020, date of publication December 4, 2020,
date of current version December 22, 2020.

Digital Object Identifier 10.1109/ACCESS.2020.3042702

Automatic Ship Recognition Chain on Satellite Multispectral Imagery

KAMIRUL KAMIRUL[1], (Member, IEEE), WAHYUDI HASBI[2], (Senior Member, IEEE), PATRIA RACHMAN HAKIM[2], AND A. HADI SYAFRUDIN[2]

[1]Satellite Control, Space and Atmospheric Observation, and Remote Sensing Office, National Institute of Aeronautics and Space, Biak 98118, Indonesia
[2]Satellite Technology Center, National Institute of Aeronautics and Space, Bogor 16310, Indonesia

Corresponding author: Wahyudi Hasbi (wahyudi.hasbi@lapan.go.id)

The publication of this work is funded by the Satellite Technology Center, the National Institute of Aeronautics and Space (LAPAN), Indonesia.

ABSTRACT This article elaborates a processing chain devised to recognize the ships existing on medium resolution multispectral imageries (MSI). The chain consists of the following three steps. Firstly, an adaptive local saliency mapping technique is instigated on open ocean regions to obtain all floating objects. Secondly, to extract the ship candidates, two-step verification is applied based on specific spectral and geometric information of the ships. Lastly, a calculation to determine the properties of the ships, including their length, breadth, and heading, is then carried out. Furthermore, we propose a novel method for correcting miscalculated ship heading; by combining wake segmentation and Radon Transform (*RT*) approaches to locate the position and estimate the length of the wake generated by the ships. With the detected wake length, ship velocity can also be assessed. The developed chain is then tested using imageries acquired by LAPAN-A3 microsatellite, and the results are compared to those reported by the Automatic Identification System (AIS). Experimental results indicate that the proposed chain achieves higher detection performance and can produce better heading information compared to the existing methods.

INDEX TERMS LAPAN-A3, satellite, medium resolution, recognition, remote sensing, ship.

I. INTRODUCTION

The presence of remote sensing techniques unlocks the ability to measure the properties of an object from a distance. The term 'object' may refer to man-made objects such as vehicles, ships, buildings, etc., or naturally existed objects, including lakes, mountains, oceans, etc [1]–[3]. Such objects' properties can be recognized by involving specific detection methods depending on the information desired to be extracted. Object detection in a remotely sensed image is a core tool that monitors environmental change, geographic information system update, open ocean monitoring, and urban planning can be continuously and automatically carried out [4]–[7].

One of the most popular applications of object recognition on remote sensing imagery is for maritime domain awareness. In this context, the imagery is used to precisely track and monitor each ship by maritime authorities. As a result, by combining fine quality imagery and a reliable developed detection algorithm, suspicious activities such as illegal fishing can be identified [8]–[12]. Another technology that can also be implemented for supporting maritime awareness service is the Automatic Identification System (AIS). AIS is an automated vessel tracking and monitoring technology operated via the electronic exchange of data with nearby vessels, ground-based systems, and satellites [13]–[14]. Nowadays, AIS is mandatory for ships with a gross tonnage of 300 or more and all commercial passenger vessels, regardless of size (based on the IMO's International Convention for the Safety of Life at Sea). As globally implemented, AIS capability is further expanded to monitor vessel activities both at sea and in ports, with numerous other applications. Some of these applications include fishing vessel fleet monitoring and control, ship traffic management, search and rescue, and maritime security [15]–[17].

Although AIS technology is reliable enough to perform ship monitoring and tracking tasks, some issues are related to this system. Since vessel operators control this system, they can manipulate the transmitted data, enlarge the transmission interval, or even disable the transmission signal [18], [19]. As a result, currently-reported dynamic parameters reaching the end-receiver side could be unrepresentative. Consequently, using those parameters as the input of

The associate editor coordinating the review of this manuscript and approving it for publication was Hongjun Su.

AIS-based tracking and monitoring activities will conduce an imprecise result. According to this particular shortcoming, ship recognition using remote sensing imagery is still becoming a predominant choice since there is no hiding place missed by the imaging device.

Generally, ship recognition in remote sensing imagery can either be carried out by using machine-assisted or automatic approaches. A machine-assisted approach is a viable option for a system supplied by a large number of imagery datasets. As demonstrated by the authors in [20], ship candidates on Google Earth and GaoFen-2 imageries can be extracted by employing a convolutional neural network (CNN). Another machine-assisted approach has also been successfully implemented by [21] after combining the AdaBoost classifier and Haar-like feature detection.

The term ''automatic recognition'' refers to a fully unsupervised process of detecting an object and calculating its associated properties without involving any previous ship-related knowledge. Compared to the machine-assisted side, this approach is more likely to be developed and delivered faster as neither the massive data collection nor the time-consuming training stage is required. Even though this approach may produce a less accurate result than the machine-assisted one, its performance can still be improved by finely optimizing the parameters involved.

Many successfully-developed automatic ship recognition on optical satellite imagery, including the work reported by authors in [22]. In their work, sea surface analysis has been employed to recognize ships existing in the various sea background, i.e., quiet, textured, and cluttered. Moreover, an automatic ship detection chain for SPOT-5 imagery combining the statistical analysis, mathematical morphology approach, and signal-processing techniques such as the wavelet analysis and Radon transform has also been successfully demonstrated by the authors [23]. Furthermore, as reported in [24], even from a geostationary distance, an automatic detection employing a local saliency map is found capable of providing a satisfying result.

This article elaborates on a processing chain developed to locate the ships existing on multispectral imageries (MSI) and to precisely determine their dynamic and static properties. The medium resolution MSI was concerned due to its wide-swath advantage, enabling wide-area ocean monitoring to become possible, even though it has limited resolution, compared to the high-resolution one which has limited swath for ocean monitoring. Therefore, in this work, we used a set of 4-band (red, green, blue, near-infrared) medium resolution MSI acquired by the LAPAN-A3 satellite for the testing purpose.

LAPAN-A3, also known as LAPAN-IPB satellite, is the third Indonesian microsatellite jointly developed by the Indonesian National Institute of Aeronautics and Space and Bogor Agriculture Institute (IPB). This satellite has been injected into polar orbit (98° of inclination) at 505 km of altitude in June 2016. One of the imaging payloads mounted to this satellite is a push-broom sensor capable of capturing a 4-band medium resolution MSI with 16m of ground sampling resolution and 122.4 km of the swath width [25]–[27].

In designing the recognition chain, we divide the process into two main stages, ship detection and properties determination of the detected ship.

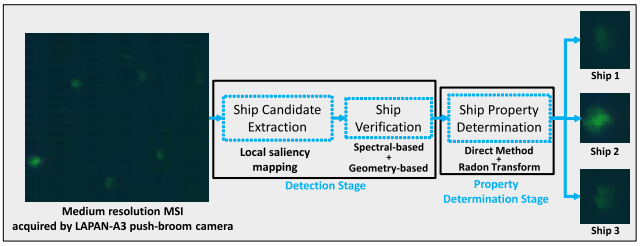

FIGURE 1. The workflow of the developed ship recognition chain.

As given in Fig. 1, the detection stage consists of two main parts, i.e., candidate extraction and verification. At the beginning of extraction, we combined ocean segmentation and a novel adaptive local saliency map approaches to locate all ship candidates. Since the chain was designed to suit the ocean input image containing cloud and land, the ocean segmentation is required to constrict the area of interest. In our work, parameters derived from the spectral characteristic of water on LAPAN-A3 MSI are sufficient to supply direct thresholding, the core of the segmentation. Meanwhile, the adaptive local saliency map approach presented in this work is the modified version of its predecessor in [24], upgraded to be independent of any predefined threshold. At the end of this stage, candidates are cropped and fed into the verification stage.

We combined spectral-based and geometry-based verification to ascertain whether a given candidate is real in the verification stage. In the beginning, the candidate's spectral response is analyzed to check whether it matches with the characteristics of reference ship spectral on LAPAN-A3 MSI. Afterward, the estimated length, breadth, and eccentricity of each given candidate are used for the geometry-based verification. A direct and fast methodology for ship recognition developed by [28] has been employed in calculating such geometries.

In addition to the recognition chain, we also proposed a method for addressing the falsely-calculated heading issue introduced by [28]. Since the method ignores the actual stern and bow position, the estimated heading sometimes has a difference of 180° from the reference. Therefore, we employed the Radon transform (*RT*) for detecting the wake generated by a sailing ship so that the actual stern position can be determined. Furthermore, we have also estimated the length of the detected wake to determine sailing speed. Accordingly, the *RT*-based correction enables the developed chain to provide also velocity-related information. Finally, we used a combined terrestrial and satellite-based AIS dataset for assessing the performance of the chain. Moreover, since the AIS dataset does not hold dimension-related information,

we also compared the calculated dimensions to the online database's references.

The rest of this article is organized as follows: First, in Section II, we explained in detail the strategies used in developing the chain. In Section III, the proposed *RT*-based heading correction and velocity estimation are presented. Finally, we provided the experimental details and results in Section IV, followed by the conclusion in Section V.

II. SHIP RECOGNITION CHAIN

This section explains the details of ocean segmentation and adaptive saliency mapping used in the extraction stage. Moreover, the explanation related to geometry and spectral-based verification is also presented. As we used 4-band (red, green, blue, near-infrared) MSI captured by the LAPAN-A3 optical sensor, the R, G, B, and N notations are respectively assigned to denote these bands in the rest of this article.

A. OCEAN SEGMENTATION

Ocean segmentation is necessary to constrict the area of interest while locating the desired ships. In the beginning, direct thresholding is applied to R band response to extract coarse ocean regions. The binary image W holding the ocean and non-ocean pixels can be obtained by applying Eq. (1) below:

$$W(i,j) = \begin{cases} 1, & R(i,j) \leq W_{th} \\ 0, & \text{else} \end{cases} \tag{1}$$

where the W_{th} refers to an empirically-determined value. If the value of R at a specific row and column (i, j) is not greater than W_{th}, it will be assigned as an ocean pixel.

In addition to ocean segmentation, a thresholding step for blocking out inadvertently segmented cloud blobs on W has also been carried out. This step is required since ship-sized clouds could be recognized as a real ship, raising the false detection rate while included in subsequent processing. Since the cloud reflectance index is relatively higher in N band than that of other objects, we used this band for locating the blobs. Eq.(2) below shows that the inverse of cloud binary image, C, can be obtained by applying an empirically-determined threshold C_{th} on N band.

$$C(i,j) = \begin{cases} 0, & N(i,j) \geq C_{th} \\ 1, & \text{else} \end{cases} \tag{2}$$

Finally, a cloud-free ocean binary image, I_{WC}, is obtained by operating pixel-wise conjunction between the W and C images.

$$I_{WC}(i,j) = W(i,j) \& C(i,j) \tag{3}$$

In Fig. 2, it is shown that the ocean regions near Jakarta Bay, Indonesia, are successfully segmented after implementing the strategy as described.

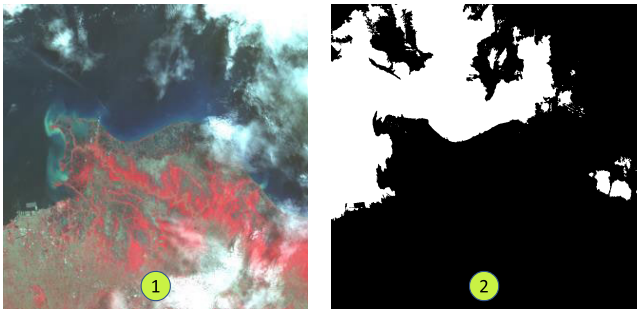

FIGURE 2. Result of ocean segmentation; (1) RGB-colored image of Jakarta taken by the LAPAN-A3 MSI optical sensor; (2) segmented ocean binary image of (1).

B. ADAPTIVE LOCAL SALIENCY MAP FOR SHIP CANDIDATE EXTRACTION

Detecting the ships on optical imagery as well as on LAPAN-A3 MSI is a challenging task since complex sea background noise could also present on the images. Moreover, in a different region of the same frame, it might be possible that the intensity of sea background is unevenly distributed; hence directly applying a global threshold for the entire pixels is inefficient for locating the ship candidates. Therefore, in this work, we introduced the adaptive local saliency mapping, an approach designed to enhance foreground objects without gaining the background noise.

The adaptive local saliency map approach introduced in this article is a modified version of the method reported in [24]. In calculating the saliency value of an individual pixel of the input image, $I(i, j)$, the neighboring pixels are involved. These pixels are categorized into two regions, background and foreground, as illustrated in Fig. 3.

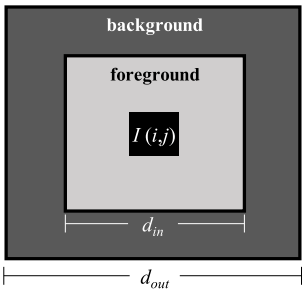

FIGURE 3. Illustration of neighboring pixels involved in the saliency map calculation.

The d_{in} and d_{out} are the spatial windows covering the inner and outer pixels centralized by $I(i, j)$. The local saliency map, S, can be obtained by following the Eq.(4) as follows:

$$S(i,j) = \frac{I(i,j) - \mu_b}{\sigma_b + eps} \tag{4}$$

the μ^b and σ^b, respectively, are the mean and standard variance of background pixels. The *eps* is introduced to compensate zero denominator cases in which is set to a small floating-point. Finally, the binary image S_B containing the

ship candidates can be extracted by thresholding the S.

$$S_B(i,j) = \begin{cases} 1, & S(i,j) > S_{th} \\ 0, & \text{else} \end{cases} \tag{5}$$

In our work, instead of manually assigning the empirically-determined S_{th} as demonstrated by the previous authors in [24], we proposed a new way to obtain this value. As we already have the I_{WC} designating the binary states of the ocean and non-ocean, we then determined the S_{th} by averaging all pixels in S that belong to the ocean. Mathematically, the S_{th} can be obtained by following Eq.(6).

$$S_{th} = \frac{\sum_{i,j}^{I_{WC}(i,j)=1} S(i,j)}{\sum_{i,j}^{=1} I_{WC}(i,j)} \tag{6}$$

Accordingly, the adaptive local saliency map approach is totally independent of any empirically-determined parameters. The only parameters used in this approach are the inner and outer window size (d_{in} and d_{out}) in which depend on the image resolution and desired size of ships to be detected. Fig. 4 provides the result after implementing the steps as explained above. It can be seen that ship candidates are successfully extracted from a noisy background input.

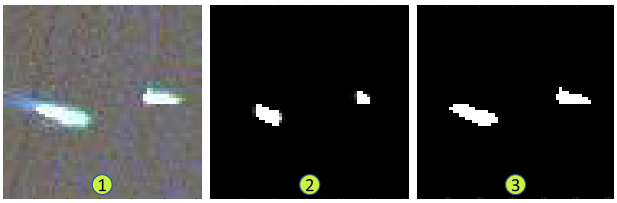

FIGURE 4. The result of applying adaptive local saliency map approach; (1) LAPAN-A3 MSI containing ships; (2) saliency image; (3) adaptively-thresholded saliency image.

C. SPECTRAL-BASED AND GEOMETRY-BASED SHIP VERIFICATION

In this section, we described the procedure for identifying and blocking out falsely-detected ships. This procedure combines spectral-based and geometry-based verification.

1) SPECTRAL-BASED VERIFICATION

In this type of verification, an analysis was performed on a limited spectral sample of ships found on LAPAN-A3 MSI to determine the appropriate spectral-related thresholds. Based on the analysis, only ships that meet at least one of the two criteria below will be included in the next processing step.

$$(\max(G^{ship}) - G_{wt}) > G_{th} \tag{7}$$

$$(\max(B^{ship}) - B_{wt}) > B_{th} \tag{8}$$

The max (G^{ship}) and max (B^{ship}), respectively, are the maximum value of pixels found on G and B bands, while G_{wt} and B_{wt} are the mean value of pixels for each of those bands. Lastly, G_{th} and B_{th} are empirically-determined values used for thresholding the G and B bands, respectively.

From the processes of ocean segmentation, candidate detection, and spectral-based verification, several parameters are empirically determined. To summarize, the definitions and values of these parameters are provided in Table 1.

TABLE 1. Empirically-determined parameters used in spectral-based verification.

Symbol	Definition	Value
W_{th}	Parameter used in detecting ocean pixels (applied on R band)	2000
C_{th}	Parameter used in detecting cloud pixels (applied on N band)	6000
G_{th}	Parameter used in verifying ship candidates (applied on G band)	2000
B_{th}	Parameter used in verifying ship candidates (applied on B band)	2000

All of the parameters in Table 1 were empirically-determined from the limited datasets used in the experiment. These parameters are sensitive to sensor setup and sun-related factors such as illumination angle. However, in our case, these values are relatively constant since the MSI used in the experiment has already been preprocessed by in-house radiometric calibration software. Satellite Technology Center of LAPAN has developed this software to compensate for the variation on digital number (DN) due to the change of sunlight intensity and sensor sensitivity. Since the LAPAN-A3 was placed in the sun-synchronous orbit and its attitude is always maintained to be in nadir during the acquisition, there is no slight change of intensity on recorded LAPAN-A3 MSI. According to these reasons, the parameters provided in Table 1 are considered to be constant. Automation in determining appropriate thresholds might be considered by involving the machine learning technique. However, this approach requires an extensive amount of MSI, followed by a complex training phase that is still not achievable in our case.

2) GEOMETRY-BASED VERIFICATION

The geometry-based verification is applied to include only the ships having a specific range of geometry. In the beginning, the length, breadth, and eccentricity of each candidate successfully passing the previous verification (spectral-based verification) are calculated. In calculating these properties, a direct method proposed by [28] has been applied to the cropped frame of the binary ship candidate image, S_B^C. To perform this method, firstly, the total number of pixels designating the ship (N_c) on S_B^C must be first calculated by using Eq.(9).

$$N_c = \sum_{i,j}^{>0} S_B^c(i,j) \tag{9}$$

Afterward, calculations to determine the center mass of the ship in x and y coordinate are carried out by employing

Eq.(10) and Eq.(11), respectively.

$$\bar{x} = \frac{\gamma}{N_c} \sum_{i,j}^{>0} i.S_B^c(i,j) \tag{10}$$

$$\bar{y} = \frac{\gamma}{N_c} \sum_{i,j}^{>0} j.S_B^c(i,j) \tag{11}$$

The γ refers to the spatial resolution of the input image, 16m for LAPAN-A3 MSI. Moreover, the covariances, the cores for geometry calculation, are also calculated by following Eq.(12) through Eq.(14).

$$\sigma_{xx}^2 = \frac{\gamma^2}{N_c} \sum_{i,j}^{>0} i^2.S_B^c(i,j) - \bar{x}^2 \tag{12}$$

$$\sigma_{yy}^2 = \frac{\gamma^2}{N_c} \sum_{i,j}^{>0} j^2.S_B^c(i,j) - \bar{y}^2 \tag{13}$$

$$\sigma_{xy}^2 = \frac{\gamma^2}{N_c} \sum_{i,j}^{>0} i.j.S_B^c(i,j) - \bar{x}.\bar{y} \tag{14}$$

Then, ship heading (θ) and eccentricity (ε) can be obtained by substituting the covariances above to Eq.(15) and Eq.(16).

$$\theta = \frac{1}{2} \tan^{-1} \left(\frac{2\sigma_{xy}^2}{\sigma_{xx}^2 - \sigma_{yy}^2} \right) \tag{15}$$

$$\varepsilon = \frac{\sigma_{xx}^2 - \sigma_{yy}^2}{\sigma_{xx}^2 + \sigma_{yy}^2} \frac{1}{\cos(2\theta)} \tag{16}$$

Finally, ship length (SL) and breadth (SB) can be calculated using Eq.(17) and Eq.(18):

$$SB = \sqrt{6(1-\varepsilon)(\sigma_{xx}^2 + \sigma_{yy}^2)} \tag{17}$$

$$SL = \sqrt{6(1+\varepsilon)(\sigma_{xx}^2 + \sigma_{yy}^2)} \tag{18}$$

Once the length and breadth are successfully calculated, the following conditions are applied to categorize a given image as a real ship.

$$SL^{\min} \leq SL \leq SL^{\max} \tag{19}$$

$$SB^{\min} \leq SB \leq SB^{\max} \tag{20}$$

$$\varepsilon^{\min} \leq \varepsilon \leq \varepsilon^{\max} \tag{21}$$

Limiting the range of length and breadth is intended to exclude relatively large objects such as small islands that are still detected if the ocean segmentation fails. This limitation can also be used for removing defected pixels detected as the objects during the saliency mapping. Moreover, by specifying the desired limit of eccentricity, the classification of elongated ship-like objects can be made. This limitation is also useful for discriminating the ships from other less-elongated objects such as icebergs, ice floes, and wind turbines. The details of the parameters and their respective values used in geometry-based verification are given in Table 2.

To be convenient with the symbol for the subsequent usages, each frame of the cropped ship successfully passing the spectral-based and geometry-based verification will be denoted as the S_{BF}.

TABLE 2. The parameters used in geometry-based verification.

Symbol	Parameter	Value
$SL^{\min}$	minimum ship length	100 m
$SL^{\max}$	maximum ship length	500 m
$SB^{\min}$	minimum ship breadth	20 m
$SB^{\max}$	maximum ship breadth	100 m
$\varepsilon^{\min}$	minimum eccentricity	0.50
$\varepsilon^{\max}$	maximum eccentricity	0.96

III. HEADING CORRECTION AND VELOCITY ESTIMATION

This section describes a method for determining true ship heading based on Radon transform (*RT*). This method has been developed to tackle the problem introduced as the existing method implemented in medium-resolution MSI. Moreover, an approach for estimating the ship velocity using its wake component is also presented.

A. RT-BASED METHOD FOR DETERMINING TRUE SHIP HEADING

Although the direct method introduced by [28] can determine ship's heading properly, it sometimes fails. Since the calculation is made based on binary pixel distribution only, the ship's bow and stern cannot be distinguished. Hence, the resulted heading (θ) could be its ambiguous pair, i.e., $\theta \pm 180°$. Therefore, an improvement in detecting and correcting this ambiguity is required.

The proposed strategy for detecting false heading requires both the frames of verified ship binary image (S_{BF}) and segmented ship-and-wake image, I_{SW}. As the S_{BF} is already provided by the verification chain, the main challenge lies in extracting the I_{SW} itself. We have found that the wake component and its associated ship can be extracted by thresholding the blue band response of S_{BF} image (B_S).

$$I_{SW}(i,j) = \begin{cases} 1, & B_S(i,j) \geq T_B \\ 0, & \text{else} \end{cases} \tag{22}$$

$$T_B = \frac{\sum_{i,j}^{S_{BF}(i,j)=0} B_S(i,j)}{\sum_{i,j}^{=0} S_{BF}(i,j)} C_B \tag{23}$$

In this case, the T_B is the mean value of ocean pixels on B_S multiplied by a weighting factor C_B. The C_B factor is included to control the sensitivity of ship-and-wake segmentation. In our work, the optimum C_B was obtained by considering the trade-off between this value and the accuracy of heading and velocity resulted. The segmentation on blue response is aimed to extract the quiet sea region reflecting less amount of blue wavelengths from other objects, including the ship and

its wake. Finally, the detection of falsely-calculated heading can be made by involving both the segmented ship-and-wake (I_{SW}) and the extracted ship candidate binary image (S_{BF}). The result of ship-and-wake segmentation is shown in Fig. 5.

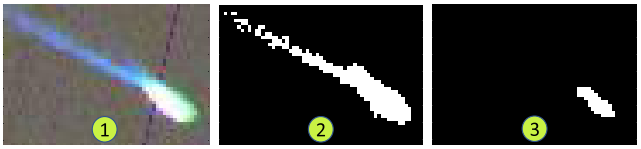

FIGURE 5. Images to be used in heading correction; (1) RGB image containing ship and wake; (2) segmented ship-and-wake binary image, I_{SW}; (3) verified ship binary image, S_{BF}.

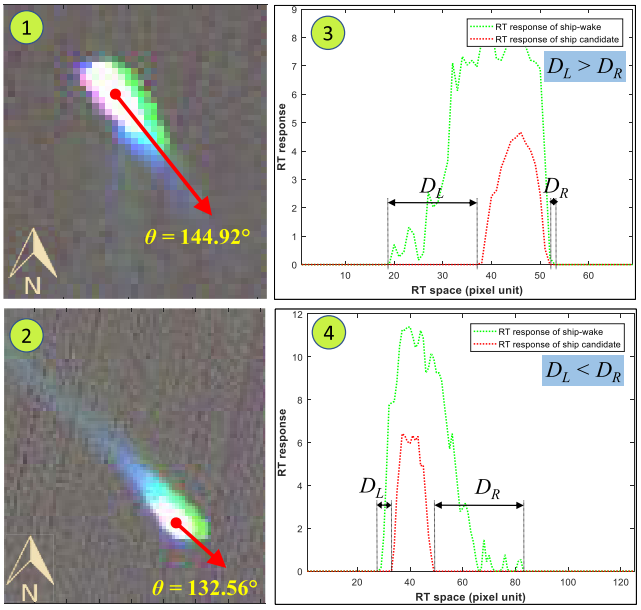

FIGURE 6. Comparison of *RT* responses generated using the falsely and correctly calculated ship heading; (1)-(2) RGB image containing the falsely and correctly calculated ship heading; (3)-(4) the *RT* responses on Radon space at $\theta - 90°$.

At the beginning of *RT*-based heading correction, the heading calculated using Eq.(15), θ, is used as the initial *RT* angle. The *RT* is then performed both on the I_{SW} and S_{BF} image at a certain angle perpendicular to the initial heading, $\theta - 90°$. If the *RT* is applied on a correctly-calculated heading I_{SW}, the wake response will always be detected on the right-hand side of the ship's center on the Radon space. On the contrary, if the same schema is applied on a falsely-calculated heading I_{SW}, the wake response will appear on the other side. By overlaying the *RT* responses generated using S_{BF} and I_{SW}, the actual side of wake can be spotted since there are offsets between these responses on both sides. As illustrated in Fig. 6, the offsets can be recognized by calculating the distances between the outermost non-zero response of I_{SW} and the S_{BF}. Both of these distances, respectively, are the margin width on the left and right-hand side of the ship denoted by D_L and D_R. In this case, the higher distance side indicates the stern location as the existence of wake contributes to the higher margin.

Finally, the corrected headings θ' can be calculated based on the D_L and D_R values by following Eq.(24).

$$\theta' = \begin{cases} \theta, & D_L \leq D_R \\ (\theta + 180°) \bmod 360°, & D_L > D_R \end{cases} \tag{24}$$

The first term of Eq. (24) tells that if the wake pattern is detected on the right-hand side of Radon space, the previously-calculated heading is already correct; hence, the correction is unnecessary. On the other hand, the correction is required to convert the heading to its ambiguity pair as the wake is detected on the left-hand side. Finally, the length of the wake λ generated by the ship is equal to the highest value between D_L and D_R multiplied by MSI spatial resolution γ. This multiplication must be carried out since the resulted D_L and D_R are stated on the pixel unit.

$$\lambda = \max([D_L D_R])\gamma \tag{25}$$

In the next section, the λ is used for determining the ship velocity.

B. VELOCITY ESTIMATION BASED ON WAKE LENGTH

This section explains the steps of estimating ship velocity based on wake length in which has been obtained in Eq.(25). In general, a sailing ship generates turbulent wake and Kelvin waves, as illustrated in Fig. 7. However, in LAPAN-A3 MSI, the Kelvin waves are entirely unobservable. Due to the absence of this wave, we used a simplified approach to estimate the transverse component of Kelvin waves (Z) from the detected turbulent wakes.

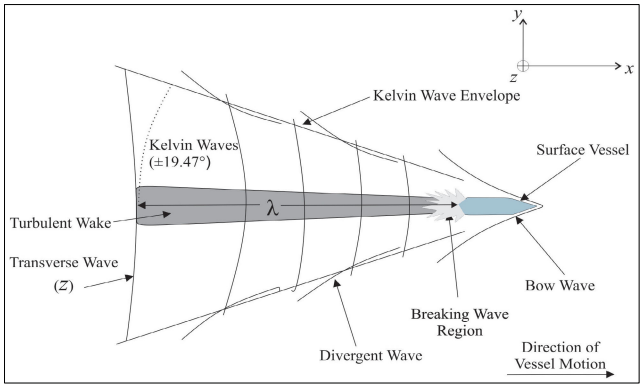

FIGURE 7. Illustration of turbulent wake and Kelvin waves generated by a sailing ship.

Fortunately, since the Kelvin waves are always bounded by cusp-lines separated by a fixed angle of 19.47° [29], the Z can be estimated by following Eq.(26).

$$Z = \lambda \tan(19.47°) \tag{26}$$

Furthermore, the equation relating the Z and ship velocity, V_{ship}, is given below [30]:

$$V_{ship} = \sqrt{\frac{Zg}{2\pi}} \tag{27}$$

where g is the gravitational constant. According to Eq.(27) above, the accuracy of the estimated velocity entirely depends on the capability of the ship-and-wake segmentation stage in extracting the wake component. Therefore, an experiment aimed to find the optimum segmentation parameter C_B is conducted and reported in Section IV.B.2.

IV. EXPERIMENTS

A. EXPERIMENTAL DATA

In order to test the developed ship recognition chain, we used three sceneries of LAPAN-A3 MSI as the input images. These imageries have been acquired in three different active ports. The details of these imageries are provided in Table 3.

TABLE 3. List of LAPAN-A3 MSI used in the experiment.

Name	Acquisition time	Target location
Image 1	May 7th, 2019 (09:19:20 – 09:20:21 UTC)	Port of Lagos, Nigeria
Image 2	May 11th, 2019 (01:52:43-01:53:25 UTC)	Port of Pasuruan, Indonesia
Image 3	September 7th, 2019 (07:48:40-07:50:13 UTC)	Port of Cape Town, South Africa

Furthermore, satellite-based AIS datasets associated with these imageries are also used to verify the dynamic parameters resulted from the chain. The satellite-based AIS was gathered from the same satellite, LAPAN-A3. Since the AIS dataset does not hold dimension-related information, we also compared the calculated lengths and breadths to references freely available on an online database, www.vesselfinder.com.

B. EVALUATION CRITERIA

In order to objectively evaluate the performance of the developed chain, we employed the *Precision* and *Recall* metrics. The *Precision* reflects the false detection rate of an algorithm, while the *Recall* represents the effectiveness of detection. *Precision* is expressed as follows:

$$Precision = \frac{N_{TP}}{N_{TP} + N_{FP}} \times 100\% \tag{28}$$

where N_{TP} and N_{FP}, respectively, are the number of correctly detected ships and the number of falsely detected ships. Meanwhile, the *Recall* of an algorithm is formulated as follows:

$$Recall = \frac{N_{TP}}{N_{TP} + N_{FN}} \times 100\% \tag{29}$$

where N_{FN} represents non-detected ships. Since we used the AIS dataset as the reference, the denominator of Eq.(29) is equal to the total number of ships reported by the AIS.

Moreover, to assess the accuracy of calculated geometries (breadths and lengths), headings, and velocities, two different metrics, i.e., mean absolute percentage error (*MAPE*) and linear regression constant (R^2) are also employed. The *MAPE* represents the amount of percentage error between the two data populations. In this work, the *MAPE* is employed for measuring the accuracy of calculated lengths and headings. The equation for calculating the *MAPE* is expressed as follows:

$$MAPE = \frac{\sum_{i=1}^{N} \frac{|x_i - r_i|}{\max(x_i, r_i)}}{N} \times 100\% \tag{30}$$

where N is the total sample, while x_i and r_i, respectively, represent the measured and the reference points.

The R^2 represents the proportion of variance in the tested variable that is predictable from its reference. In our case, the R^2 is used for measuring the strength of the relationship between the resulted parameters and their references. In the linear regression case, the R^2 of a given (x, r) pair can be calculated by following Eq.(31).

$$R^2 = \frac{\sum_{i=1}^{N} (x_i - \bar{x})^2}{\sum_{i=1}^{N} (x_i - r_i)^2} \tag{31}$$

C. RESULTS AND PERFORMANCE

This section explains the results achieved by implementing the developed ship recognition chain. In addition to the results, the capabilities and limitations of the chain are also discussed. At the end of this section, we also provided a performance comparison between the developed chain and methods presented in [22] and [24].

It should be noted that the rest of the results reported in this article has been obtained by assigning fixed d_{in} and d_{out} values in the ship detection stage. These values were chosen according to the experiment results as provided in Fig. 8.

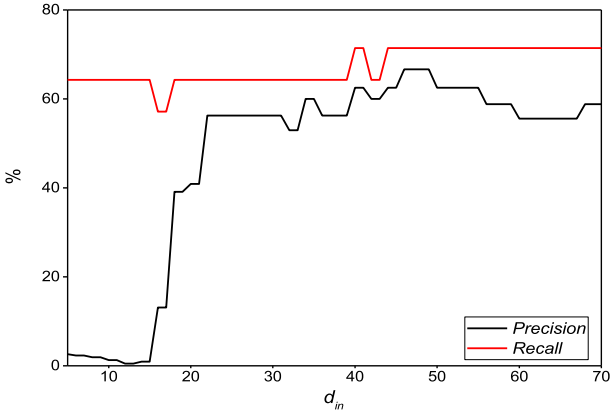

FIGURE 8. The *Precision-Recall* response as the sizes of the windows is varied.

The *Precision-Recall* curve in Fig. 8 was obtained by assigning the d_{out} to 20 pixels larger than d_{in} to keep the background window has wider coverage than that of the foreground. According to the plot, we have found that the d_{in} and d_{out} equal to 46 and 66 can result in the highest detection performance; hence, these values are then assigned as

TABLE 4. Properties of ships correctly-detected by the developed chain.

Ship ID	MMSI	Length (m)	Breadth (m)	Heading (°)	Velocity (knot)
1	477014600	260.0	32.0	31.9	18.40
2	636018687	176.0	31.0	208.0	0.00
3	636016364	146.0	26.0	192.3	0.15
4	636019263	175.0	33.0	218.0	0.00
5	538002088	228.0	32.0	212.0	0.00
6	376164000	181.0	27.0	210.0	0.10
7	538005140	144.0	23.0	199.0	0.20
8	240069000	229.0	42.0	308.0	1.30
9	354175000	186.0	30.0	221.0	0.20
10	636016281	150.0	22.0	56.2	0.70
11	210916000	178.0	28.0	131.0	1.80
12	255806075	221.0	30.0	122.0	13.00
13	353220000	179.0	28.0	101.0	0.10
14	525003620	196.0	30.0	91.0	10.70
15	563950000	360	65	284.7	16
16	538008190	330	60	138.5	13.6
17	636015119	274	48	331.6	14.6
18	636015304	275	48	329.2	13.9
19	256588000	292	45	168.6	12.2
20	354623000	289	45	115.3	10.9
21	374062000	330	57	350	13.5
22	636014118	190	32	343.4	0.2
23	636018475	290	47	351	0.1
24	477271100	292	45	102.7	10.8
25	209889000	229	37	90	10.4
26	414742000	225	32	113.7	9.3
27	209422000	225	32	187	0.1
28	351305000	189	31	106	0

the optimum sizes of windows. For analysis, the static and dynamic properties of ships correctly detected by implementing optimum d_{in} and d_{out} are shown in Table 4. These properties were obtained from AIS dataset and online ship database.

All of the ships above are used as references in assessing the performance of the developed method.

1) RESULTS ON POSITIONING ACCURACY AND CALCULATED SHIP DIMENSIONS

This section explains the accuracy of the developed chain in locating the ships and determining the lengths and breadths of the ship.

a: POSITIONING ACCURACY BY THE DEVELOPED CHAIN

In order to evaluate chain accuracy in locating the ships, the geographic distance between the detected and the reported location is calculated. The calculation was made possible by implementing the Haversine formula, requiring two latitude-longitude pairs as the input. Fig. 9 shows the distance distribution in which is stated as ''positioning error'' on the rest of this article.

The results presented in Fig. 9 were obtained after a correction schema for compensating the difference between image acquisition time and AIS timestamp applied. As a result, the reported position used in calculating the positioning error was previously interpolated based on their time difference and the currently-reported dynamic parameters.

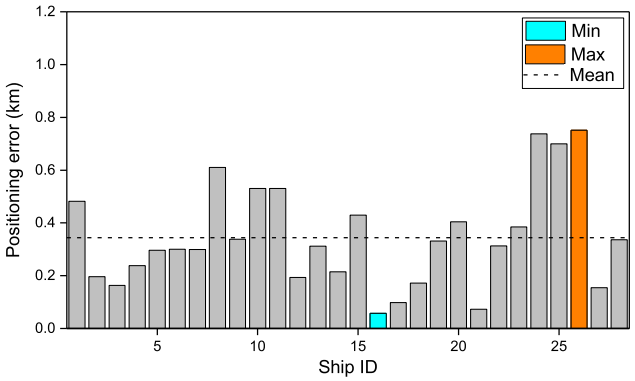

FIGURE 9. Distribution of ships positioning error.

According to Fig. 9, it is confirmed that the developed chain is capable of accurately locating the ships on the given images. It is shown that the error, is ranging from 57 to 750 m with an average value of 344 m. As the reported AIS position has already been corrected, the current positioning error is most likely caused by inaccurate ground control points (GCPs) assigned during the geo-referencing stage. In general, it is difficult to assign precise GCPs, especially for ocean areas in which unique features or objects are rarely found. Therefore, the accuracy of GCPs, in our case, influences the capability of the developed chain in locating the ships.

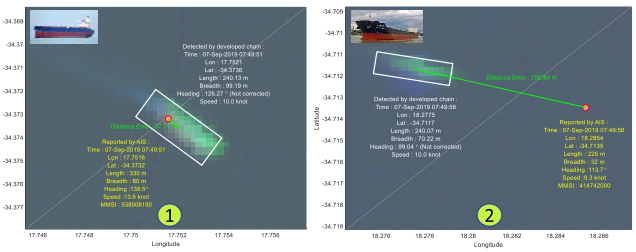

FIGURE 10. Ships having the smallest and largest positioning error (Ship photos downloaded from http://www.shipspotting.com/gallery/photo.php?lid = 3149019 and http://www.shipspotting.com/gallery/photo.php?lid = 2344417).

In Fig. 10, we visualized two contrast conditions in which the lowest and highest positioning errors are found.

In Fig. 10 (1), a Marshall Island-flagged container ship, Front Discovery, with MMSI number 538008190, was accurately spotted by the detection chain nearby the Port of Cape Town. While in Fig. 10 (2), Yu Xiao Feng, a Chinese bulk carrier with MMSI number 414742000, was detected with the highest error of up to 750m located by the developed chain. Although the chain produces the highest positioning errors on this particular ship, the other parameters, such as length, speed, and heading, have been precisely calculated. Therefore, a relatively high positioning error resulted from the chain is still acceptable since this error is directly affected by the non-chain-related issue, i.e., the quality of geo-referenced images.

b: ACCURACY ON CALCULATED SHIP DIMENSIONS

Despite optimum d_{in} and d_{out} have been used in the chain, an unstable relationship between the calculated lengths and those found in references still exists. As provided in Fig. 11, the calculated lengths swing around the references depends on the image fed to the chain. It is shown that the lengths extracted from "Image 1" and "Image 2" tend to exceed their references. On the contrary, the calculated lengths found in "Image 3" are relatively smaller than that of the references. From this plot, it is confirmed that the calculated lengths in "Image 1" are relatively closer to their references than that found on other images.

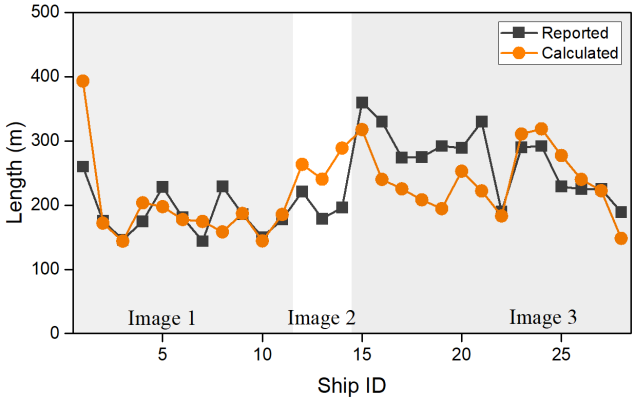

FIGURE 11. Comparison of calculated and reported lengths.

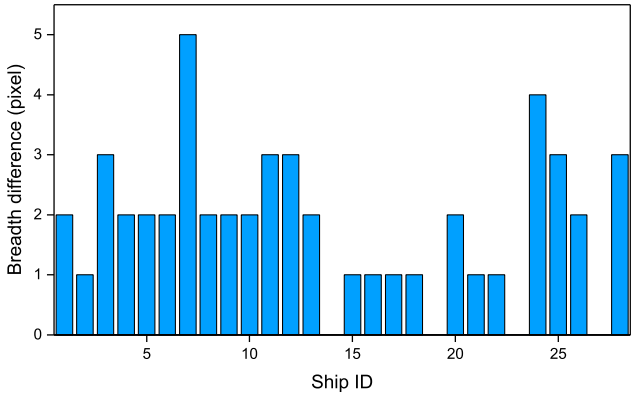

FIGURE 12. Breadth difference in the pixel unit.

As experienced by the lengths, the difference between the calculated and reported breadths are also found. As shown in Fig. 12, the error between these breadths ranges from 1 to 5 pixels with an average value of 1.8 pixels, which is still in an acceptable range of error.

To analyze the error of calculated dimensions, in Fig. 13, we provided the *MAPE* of dimensions in which representing the percentage error between the calculated and reported dimensions.

According to Fig. 13, the highest error of lengths and breadths are both found in "Image 2" then followed by

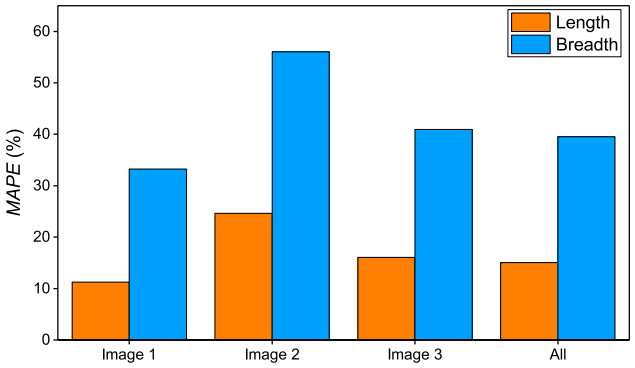

FIGURE 13. *MAPE* of dimensions for different test images.

"Image 3" and "Image 1." It is also shown that the overall *MAPE* of lengths and breadths is around 15.1% and 35.9%, respectively. Moreover, it is clear that the *MAPE* of lengths covary with the *MAPE* of breadths. As inspected on the input image individually, the *MAPE* of breadths increases as the *MAPE* of lengths gets larger. This phenomenon indicates that the factors influencing the *MAPE* of lengths also affecting the performance of the chain in estimating the breadths, and those factors depend on the quality of input images.

In addition to *MAPE* of dimensions, it is also found an interesting result related to the accuracy of calculated breadths. As shown in Table 5, the larger the true breadths, the lower the *MAPE* resulted. This inversely-proportional relationship indicates that the accuracy of calculated breadth actually depends on the ships' actual size. Consequently, a smaller vessel would have a larger relative error due to the limited resolution of the images.

TABLE 5. The values of *MAPE* of breadth for three different classes of true reference.

Range of breadth (m)	*MAPE* of breadth (%)
20 – 35	40.80
36 – 50	39.11
51 – 65	33.32

Due to the relatively high error found in calculated dimensions, it can be concluded that the improvement for achieving a better result is still required. In our case, this error is caused by two interrelated factors. Firstly, as commonly found on medium resolution imagery, the blur effect is unavoidable in LAPAN-A3 MSI. This effect affects the accuracy of calculated dimensions as the blurry ship image fed into the ship properties determination stage. Secondly, since we only used medium resolution imageries with a pixel resolution of 16m, a small error is difficult to be achieved as long as the results are compared to meter-unit references. However, if measured discretely in the pixel unit, the averaged error for lengths and breadths are 2.6 and 1.8 pixels, respectively. These results indicate that the calculated ship dimensions are

still acceptable despite medium resolution imagery used as the input.

Finally, we have also found that both the positioning error and the accuracy of the calculated dimensions discussed above are affected by the current sailing speed, as presented in Table 6.

TABLE 6. Positioning error and *MAPE* of dimension for two different classes of ship velocity.

Ship velocity (knot)	Average positioning error (m)	*MAPE* of length (%)	*MAPE* of breadth (%)
0 – 1.8	333.53	9.88	21.05
9.30 – 18.40	357.29	32.71	47.35

As the positioning error represents the distance between the detected and the interpolated AIS location, a fast-moving ship will produce a relatively high error since its interpolated position's uncertainty tends to increase. Therefore, on average, the ships moving with 0 – 1.8 knots can be located more precisely compared to those moving at a higher speed. In addition to positioning error, the *MAPE* of lengths and breadths also increases as the ship gets faster. This phenomenon happened since the ship moving with a higher speed will produce more wakes and ripples surrounding its hull compared to the moored one. Consequently, this problem will affect the performance ship detection stage in classifying desired ship pixels from a given ship image. As a result, the calculated lengths and breadth derived from this frame might be overestimated, resulting in a relatively larger *MAPE* value.

2) RESULTS ON HEADING AND VELOCITY

The accuracy of resulted headings and velocities depends on the ship-and-wake segmentation performance controlled by the sensitivity parameter, C_B. According to Eq.(22) dan Eq.(23), the value of C_B is inversely proportional to the number of segmented ship pixel. An extremely low C_B results in an over-estimated wake length of the ship. On the contrary, choosing a relatively high C_B may lead to the absence of detected wake; hence heading correction cannot be performed, and ship velocity will be saturated at 0 knots or anchoring. Therefore, the selection of C_B is important to be considered to provide a satisfying result. In finding the optimum C_B, we have varied this value from 0.50 to 1.50 for each image and measured the resulted *MAPE* of headings and velocities as given in Fig. 14. It should be noted that the headings provided in Fig. 14 are the corrected version as the *RT*-based approach is included by default.

Based on Fig. 14, the optimum C_B values resulting in the lowest *MAPE* of headings and velocities vary for each image. However, these values tend to range from 1.02 to 1.10. It is also shown that applying the C_B outside this range leads the *MAPE* to increase before saturated at a certain point.

According to results on Fig. 14, we set $C_B = 1.08$ for "Image 1" and "Image 3" while $C_B = 1.10$ is applied for

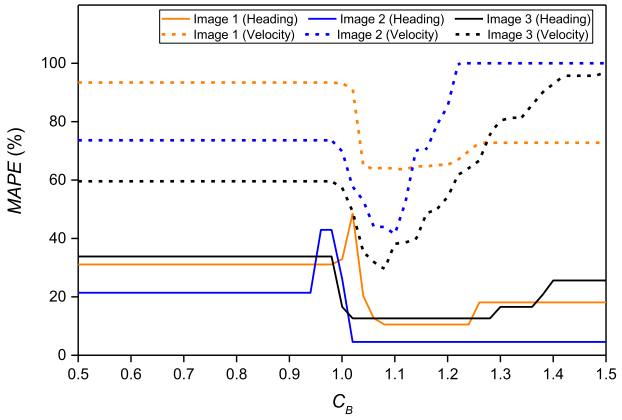

FIGURE 14. Distribution of *MAPE* of headings and velocities as the C_B varied.

"Image 2." As an in-house developed chain preprocesses the images fed to the detection chain, the extreme variation of digital number (*DN*) due to weather or light change can be compensated. As a result, even the C_B is experimentally investigated based on a limited number of images, the C_B ranging from 1.08 to 1.10 is reasonable to be assigned to a new database. We expand this part into two respective sections to deeply analyze the accuracy of resulted headings and velocities using those optimum C_B.

a: HEADINGS ACCURACY AND RT-BASED CORRECTION

In this section, we analyzed the accuracy of the chain in estimating the headings. Moreover, the comparison of accuracies and errors resulted before and after applying the *RT*-based correction are also presented.

Fig. 15 shows the correlation between corrected headings and their references.

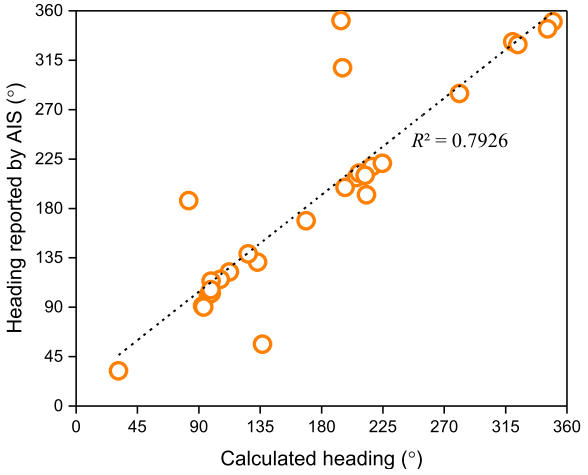

FIGURE 15. Linear correlation between corrected and reported headings.

Based on Fig. 15, the calculated headings are closely matched to those reported by AIS. Referring to the linear regression fit, the R^2 reaches up to 0.79, indicating that the

developed chain can produce a satisfying headings result. Finally, based on the resulted *MAPE* and R^2, it is confirmed that the optimum C_B is not only capable of producing the lowest percentage error but also providing a high accuracy result.

High accuracy headings achieved in this experiment is an obvious contribution from the *RT*-based heading correction. To compare the headings resulted from the direct method in [28] and the proposed *RT*-based approach, we have provided the plot of these values in Fig. 16.

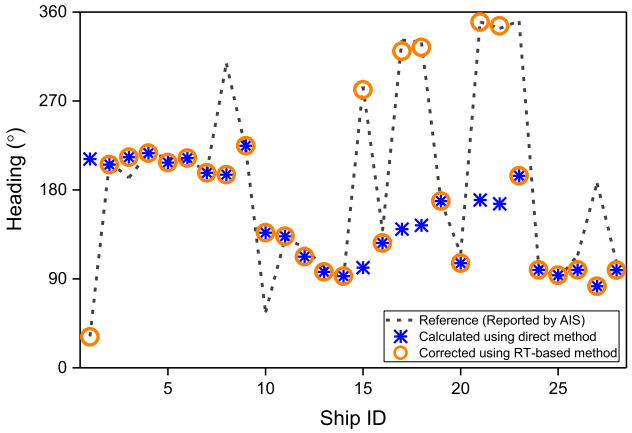

FIGURE 16. Comparison of uncorrected and corrected ship headings.

By observing the comparison plot in Fig. 16, it is shown that 6 of 28 headings (21.42%) are successfully corrected. As a result, the corrected headings are more likely closer to their references than that of the uncorrected one. To quantitatively compare these headings, we provided their *MAPE* and R^2 values in Table 7.

TABLE 7. *MAPE* of headings and R^2 of test images.

Input	*MAPE* (%)		R^2	
	Direct	Direct + *RT*	Direct	Direct + RT
Image 1	18.06	10.54	0.22	0.70
Image 2	4.42	4.42	0.99	0.99
Image 3	30.42	10.81	0.52	0.81
Overall	22.80	10.04	0.15	0.79

As individually assessed using Table 7, it is confirmed that, in general, the inclusion of the *RT*-based approach is not only capable of reducing the errors but also produces more accurate results as the R^2 coefficients are found increasing. However, a particular case is found on headings extracted from "Image 2" in which none of them are falsely-calculated, indicating that the method introduced by [28] performs perfectly in this particular image. By excluding the "Image 2," it is clear that the highest *MAPE* reduction is around 19.61% as found in "Image 3." At the same time, the highest increase in R^2 is found on "Image 1" with a value of 0.48.

b: ACCURACY OF ESTIMATED VELOCITIES

This section explains the accuracy of estimated velocities in which were calculated by making the full use of detected wake length information. As shown in Fig. 17, it is found that estimated velocities and their AIS references are in satisfying correlation with a value of R^2 up to 0.73. This result indicates that even if using medium-resolution imagery and a relatively simple approach (during the absence of Kevin wake), well-correlated velocities still can be achieved.

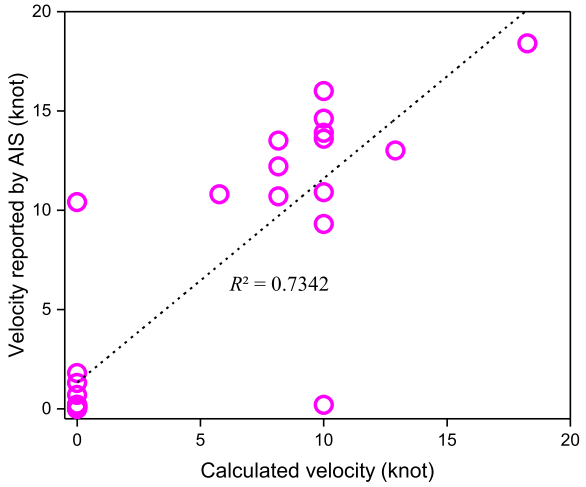

FIGURE 17. Linear regression of ship velocities.

Theoretically, by using 16m of resolution on Eq.(26), the minimum non-zero velocity, V_{MIN}, can be detected by this chain of around 5.78 knots. It means, a sailing ship having a velocity below this value will be detected as an anchoring vessel. This condition is exactly found in the results provided in Fig. 18. It can be seen that 14 of 28 ships have velocities below the V_{MIN} and are detected as in moored.

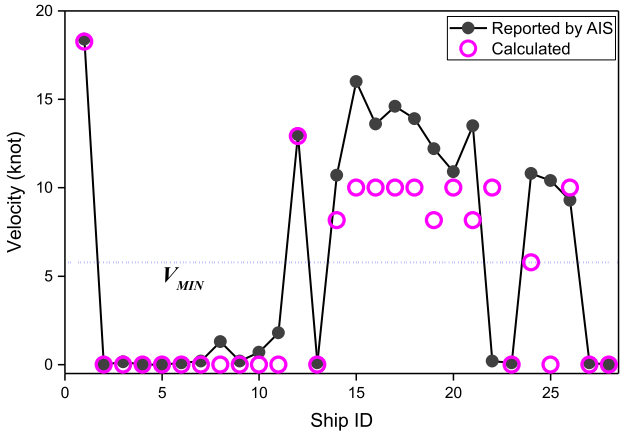

FIGURE 18. Comparison of calculated and reported velocities.

According to Fig. 18, by using LAPAN-A3 MSI, the developed chain is suitable to be used as a maritime monitoring tool for a specific area in which the ships were sailing with

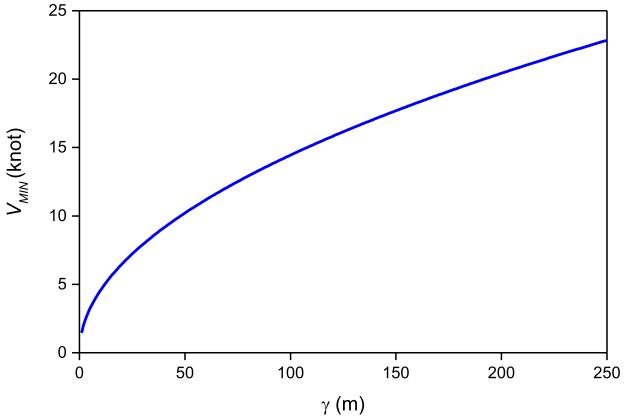

FIGURE 19. The relation between spatial resolution and the minimum ship velocity (V_{MIN}) can be detected by the developed chain.

a minimum speed of 5.78 knots. For other types of MSI, this approach can also be implemented; however, one has to consider that the V_{MIN} increases as a wider spatial resolution MSI is used. Fig. 19 shows the relation between the spatial resolution (γ) and minimum velocity recognized by the developed method (V_{MIN}).

The spatial resolution, γ, in Fig. 18 is limited to 250 m since locating a ship having breadth and length above this limit is almost impossible. Based on this plot, an image with 150 m of spatial resolution can still be used to distinguish between anchoring and sailing tanker or bulk carrier ship at a speed of 13-17 knots. However, for the imagery with a spatial resolution higher than this, only container and cruise ships moving with full speed at 16-30 knots will be detected.

The main limitation of implementing the *RT*-based for determining actual ship headings and using the wake length to estimate the velocities is that they depend on the detected wake component's availability. It means that an anchoring ship heading might not be representative if detected using the developed chain. To address the limitation on determining ship headings, one can develop a ship bow-stern discriminator algorithm. However, one must conceive that this approach requires a sufficient ground resolution MSI. Moreover, since the absence of the detected causes the velocity to be saturated at zero, choosing an appropriate C_B is essential to determine actual headings and velocities.

3) PERFORMANCE COMPARISON

This section provided the comparison results between the developed chain and methods proposed by authors in [22] and [24]. The authors in [22] used sea surface analysis for locating ships on high-resolution SPOT-5 and Google Earth service images. Then, a linear function combining pixel and region characteristics is employed to select ship candidates. Finally, two geometry-based metrics, compactness and length-width ratio, were adopted to remove falsely-detected ships. The authors in [24] employed a local saliency map to detect ships in a single frame of GF-4 satellite sequential images. However, the saliency map was generated by applying fixed S_{th} so that the final result depends on the value assigned. In Table 8, it is shown that the performance of the developed chain implementing adaptively-determined S_{th} is close to those resulted from its predecessor in [24]. This result indicates that the proposed approach is useful in reducing the effort in finding appropriate S_{th} as a new database fed into this chain.

TABLE 8. Performance comparison between the developed chain and other approaches.

Method	S_{th}	*Precision* (%)	*Recall* (%)	Running Time (second/image)
The developed chain	Adaptive	66.67	71.43	70.66
Developed chain using fixed S_{th} as firstly introduced in [24]	5	18.18	71.43	68.40
	10	62.50	71.43	68.93
	15	62.50	71.43	68.91
	20	60.00	64.29	68.87
	25	64.29	64.29	68.86
	30	56.25	64.29	68.87
The method in [22]	-	28.21	78.57	57.51

In our case, the method in [22] did not give a satisfying performance as applied on medium resolution LAPAN-A3 MSI. Compared to the developed chain, the *Precision* of this method is far behind even it has a slightly higher *Recall*. Since a low *Recall* represents an algorithm's weakness in dealing with the falsely-detected object, it can be concluded that employing the compactness and length-width ratio for detecting false alarms is less suitable to be applied in medium resolution MSI, especially for LAPAN-A3 MSI. Therefore, limiting the desired ship's dimensions to a specific range of values as used in the developed chain is necessary for achieving better performance on medium resolution MSI. Despite having a low *Precision*, the method in [22] ran 22% faster than the developed chain. This indicates that this method gives an advantage in processing speed as employed either in medium or high-resolution imagery. Based on this particular comparison, it can be concluded that the developed chain is more suitable to be implemented for recognizing the ship in the medium resolution of LAPAN-A3 MSI or other typical medium resolution imager satellites.

V. CONCLUSION

In this article, we proposed an automatic processing chain used for recognizing the ships existing on medium resolution LAPAN-A3/LAPAN-IPB MSI. The chain consisted of two main stages, i.e., ship detection and properties determination of the detected ship.

The detection algorithm was designed to extract ship candidates and to verify them. We developed an adaptive local saliency mapping technique to detect the candidates, independent of any predefined threshold. In verifying the candidates, we applied two-stage verification based on their spectral and geometry information.

The properties determination stage was carried out to estimate the length, breadth, eccentricity, and heading of the

detected ships. The estimation was made possible by implementing an existing direct-and-fast methodology for ship recognition. Finally, we also proposed a novel method based Radon transform (*RT*) to identify the actual orientation so that the accuracy of the estimated headings can be improved. This method works by comparing the response of segmented ship-and-wake and ship binary images on Radon space to obtain the generated wake's location and length. Moreover, by using the wake length information, ship velocity is also estimated.

Based on the experiments, it is found that the developed chain is capable of precisely locating the ship with an accuracy of up to 57 m as applied on 16m resolution of LAPAN-A3 MSI. It is also found that the estimated lengths and breadths are in a close match to their references with an averaged error of 2.6 pixels only. Furthermore, it is confirmed that the estimated velocities and their AIS references are in promising correlation with the value of R^2 up to 0.73. Moreover, the proposed *RT*-based method significantly improves the chain accuracy after successfully detecting and correcting 21.42% of falsely-calculated headings. Finally, compared to the existing methods, the developed chain has a higher *Precision* indicating the chain dealing well with falsely-detected objects on a medium resolution MSI.

ACKNOWLEDGEMENT

The authors gratefully thank the Satellite Technology Center, the Indonesian National Institute of Aeronautics and Space (LAPAN), for providing necessary imageries and space-based AIS datasets for this research.

REFERENCES

[1] U. Kanjir, H. Greidanus, and K. Oštir, "Vessel detection and classification from spaceborne optical images: A literature survey," *Remote Sens. Environ.*, vol. 207, pp. 1–26, Mar. 2018.

[2] G. Cheng and J. Han, "A survey on object detection in optical remote sensing images," *ISPRS J. Photogramm. Remote Sens.*, vol. 117, pp. 11–28, Jul. 2016.

[3] C. Huang, Y. Chen, S. Zhang, and J. Wu, "Detecting, extracting, and monitoring surface water from space using optical sensors: A review," *Rev. Geophys.*, vol. 56, no. 2, pp. 333–360, Jun. 2018.

[4] D. Al-Alimi, Y. Shao, R. Feng, M. A. A. Al-Qaness, M. A. Elaziz, and S. Kim, "Multi-scale geospatial object detection based on shallow-deep feature extraction," *Remote Sens.*, vol. 11, no. 21, pp. 2525–2543, Oct. 2019.

[5] P. K. Mallupattu and J. R. S. Reddy, "Analysis of land use/land cover changes using remote sensing data and GIS at an urban area, Tirupati, India," *Sci. World J.*, vol. 2013, pp. 1–6, Apr. 2013.

[6] Y. Yu, H. Guan, D. Li, T. Gu, E. Tang, and A. Li, "Orientation guided anchoring for geospatial object detection from remote sensing imagery," *ISPRS J. Photogramm. Remote Sens.*, vol. 160, pp. 67–82, Feb. 2020.

[7] I. R. Hegazy and M. R. Kaloop, "Monitoring urban growth and land use change detection with GIS and remote sensing techniques in Daqahlia governorate Egypt," *Int. J. Sustain. Built Environ.*, vol. 4, no. 1, pp. 117–124, Jun. 2015.

[8] M. Fournier, R. C. Hilliard, S. Rezaee, and R. Pelot, "Past, present, and future of the satellite-based automatic identification system: Areas of applications (2004–2016)," *WMU J. Maritime Affairs*, vol. 17, no. 3, pp. 311–345, Sep. 2018.

[9] M. Reggiannini, M. Righi, M. Tampucci, A. L. Duca, C. Bacciu, L. Bedini, A. D'Errico, C. D. Paola, A. Marchetti, M. Martinelli, C. Mercurio, E. Salerno, and B. Zizi, "Remote sensing for maritime prompt monitoring," *J. Mar. Sci. Eng.*, vol. 7, no. 7, p. 202, Jun. 2019.

[10] S. Brusch, S. Lehner, T. Fritz, M. Soccorsi, A. Soloviev, and B. van Schie, "Ship surveillance with TerraSAR-X," *IEEE Trans. Geosci. Remote Sens.*, vol. 49, no. 3, pp. 1092–1103, Mar. 2011.

[11] A. Kurekin, B. Loveday, O. Clements, G. Quartly, P. Miller, G. Wiafe, and K. A. Agyekum, "Use of sentinel-l and sentinel-2 for monitoring illegal fishing off ghana," in *Proc. IEEE Int. Geosci. Remote Sens. Symp. (IGARSS)*, Valencia, Spain, Jul. 2018, pp. 6875–6878.

[12] N. Fridman, D. Amir, Y. Douchan, and N. Agmon, "Satellite detection of moving vessels in marine environments," in *Proc. Conf. Innov. Appl. Artif. Intell.*, 2019, pp. 9452–9459.

[13] E. Tu, G. Zhang, L. Rachmawati, E. Rajabally, and G.-B. Huang, "Exploiting AIS data for intelligent maritime navigation: A comprehensive survey from data to methodology," *IEEE Trans. Intell. Transp. Syst.*, vol. 19, no. 5, pp. 1559–1582, May 2018.

[14] W. Hasbi, Kamirul, M. Mukhayadi, and U. Renner, "The impact of space-based AIS antenna orientation on in-orbit AIS detection performance," *Appl. Sci.*, vol. 9, no. 16, pp. 3319–3337, Aug. 2019.

[15] T. Eriksen, G. Høye, B. Narheim, and B. J. Meland, "Maritime traffic monitoring using a space-based AIS receiver," *Acta Astronautica*, vol. 58, no. 10, pp. 537–549, May 2006.

[16] W. Hasbi and Kamirul, "Tracking capability and detection probability assessment of space-based automatic identification system (AIS) from equatorial and polar orbiting satellites constellation," *IEEE Access*, vol. 8, pp. 184120–184136, 2020.

[17] E. Lee, A. J. Mokashi, S. Y. Moon, and G. Kim, "The maturity of automatic identification systems(AIS) and its implications for innovation," *J. Mar. Sci. Eng.*, vol. 7, no. 9, pp. 287–303, Aug. 2019.

[18] F. Mazzarella, M. Vespe, A. Alessandrini, D. Tarchi, G. Aulicino, and A. Vollero, "A novel anomaly detection approach to identify intentional AIS on-off switching," *Expert Syst. Appl.*, vol. 78, pp. 110–123, Jul. 2017.

[19] J. H. Ford, D. Peel, D. Kroodsma, B. D. Hardesty, U. Rosebrock, and C. Wilcox, "Detecting suspicious activities at sea based on anomalies in automatic identification systems transmissions," *PLoS ONE*, vol. 13, no. 8, pp. 1–13, Aug. 2018.

[20] F. Bi, J. Hou, L. Chen, Z. Yang, and Y. Wang, "Ship detection for optical remote sensing images based on visual attention enhanced network," *Sensors*, vol. 19, no. 10, pp. 2271–2283, May 2019.

[21] Y. Yu, H. Ai, X. He, S. Yu, X. Zhong, and M. Lu, "Ship detection in optical satellite images using Haar-like features and periphery-cropped neural networks," *IEEE Access*, vol. 6, pp. 71122–71131, 2018.

[22] G. Yang, B. Li, S. Ji, F. Gao, and Q. Xu, "Ship detection from optical satellite images based on sea surface analysis," *IEEE Geosci. Remote Sens. Lett.*, vol. 11, no. 3, pp. 641–645, Mar. 2014.

[23] C. Corbane, L. Najman, E. Pecoul, L. Demagistri, and M. Petit, "A complete processing chain for ship detection using optical satellite imagery," *Int. J. Remote Sens.*, vol. 31, no. 22, pp. 5837–5854, Dec. 2010.

[24] L. Yao, Y. Liu, and Y. He, "A novel ship-tracking method for GF-4 satellite sequential images," *Sensors*, vol. 18, no. 7, pp. 2007–2020, Jun. 2018.

[25] C. T. Judianto and E. N. Nasser, "The analysis of LAPAN-A3/IPB satellite image data simulation using high data rate modem," *Procedia Environ. Sci.*, vol. 24, pp. 285–296, Jan. 2015.

[26] K. Arai, W. Hasbi, A. Hadi, P. Rachman, S. Salaswati, L. Budi, and Y. Setiawan, "Method for uncertainty evaluation of vicarious calibration of spaceborne visible to near infrared radiometers," *Int. J. Adv. Comput. Sci. Appl.*, vol. 10, no. 1, pp. 387–393, 2019.

[27] P. R. Hakim, A. H. Syafrudin, S. Salaswati, S. Utama, and W. Hasbi, "Development of systematic image preprocessing of LAPAN-A3/IPB multispectral images," *Int. J. Adv. Studies Comput. Sci. Eng.*, vol. 7, no. 10, pp. 9–18, 2019.

[28] H. Heiselberg, "A direct and fast methodology for ship recognition in sentinel-2 multispectral imagery," *Remote Sens.*, vol. 8, no. 12, pp. 1033–1043, Dec. 2016.

[29] B. Tings, A. Pleskachevsky, D. Velotto, and S. Jacobsen, "Extension of ship wake detectability model for non-linear influences of parameters using satellite based X-band synthetic aperture radar," *Remote Sens.*, vol. 11, no. 5, pp. 563–582, Mar. 2019.

[30] A. Panico, M. D. Graziano, and A. Renga, "SAR-based vessel velocity estimation from partially imaged kelvin pattern," *IEEE Geosci. Remote Sens. Lett.*, vol. 14, no. 11, pp. 2067–2071, Nov. 2017.

KAMIRUL KAMIRUL (Member, IEEE) received the B.S. degree in physics from Tanjungpura University, Indonesia, in 2014, and the M.S. degree in physics from the Institut Teknologi Bandung, Indonesia, in 2017. He is currently an Engineer with the Indonesian National Institute of Aeronautics and Space. His research interest includes the parallel computing and satellite image processing. He was a recipient of the Indonesian Endowment Fund for Education Scholarship from the Indonesian Ministry of Finance in 2015.

WAHYUDI HASBI (Senior Member, IEEE) received the bachelor's degree in physics from Hasanuddin University in 2000, the master's degree in computer science from IPB University, Indonesia, in 2011, and the Ph.D. degree from the Institut für Luft-und Raumfahrt, Technische Universität Berlin, in 2020. He is currently a Senior Researcher and a Coordinator/Head of Dissemination Division, Satellite Technology Center, National Institute for Aeronautics and Space (LAPAN), Indonesia. He was involved as a System and a Chief Engineer in microsatellite projects in Indonesia, including LAPAN-TUBSAT, LAPAN-A2/LAPAN-ORARI, and LAPAN-A3/IPB. He actively involves in research and publishes articles related to the field of satellite technology. He is a Senior Member of the IEEE Aerospace and Electronic Systems Society, IEEE Geoscience and Remote Sensing Society, and the IEEE Technology and Engineering Management Society. He was elected as an IEEE Indonesia Section Chair-Elect for 2021. In 2016, he received a prestigious medal award of Satyalancana Wirakarya (''Role Model Medal'') from the President of Republic Indonesia, which was specially awarded for Outstanding Dedication in Satellite Design and Development and Became A Role Model in The Satellite Technology Development to The Country. He served as the Vice-Chair for the IEEE Indonesia Section from 2017 to 2019.

PATRIA RACHMAN HAKIM received the bachelor's and magister's degrees in electrical engineering from the Bandung Institute of Technology in 2004 and 2008, respectively.

He has research interests in digital signal processing, applied mathematics, a control system, and artificially intelligent. He is currently with the Satellite Technology Center of National Institute of Aeronautics and Space, where he leads the Satellite Mission Operation Research Group. His recent works and publications are mostly related to the development of an autonomous system for satellite operation management and satellite data processing.

A. HADI SYAFRUDIN received the bachelor's degree in electronics engineering with the Sepuluh Nopember Institute of Technology in 2005 and the master's degree in information technology for natural resources management from IPB University in 2012.

Since 2013, he has been a Researcher with the Satellite Technology Center of National Institute of Aeronautics and Space. His recent works and publications are mostly related to satellite payload instrumentation and data processing.